Journal of Minerals and Materials Characterization and Engineering, 2026, 14(3), 69-80
https://www.scirp.org/journal/jmmce
ISSN Online: 2327-4085
ISSN Print: 2327-4077

High-Temperature Stress-Strain Behavior and Fractographic Characterization of Additively Manufactured Inconel 939

Daniel Moreno, Matan Zakai, Yohanan Nahmana, Ariel Y. Cohen, Moshe Shapira

Bet Shemesh Engines Ltd., Bet Shemesh, Israel
Email: danielm@bsel.co.il

How to cite this paper: Moreno, D., Zakai, M., Nahmana, Y., Cohen, A.Y. and Shapira, M. (2026) High-Temperature Stress-Strain Behavior and Fractographic Characterization of Additively Manufactured Inconel 939. *Journal of Minerals and Materials Characterization and Engineering*, **14**, 69-80.
https://doi.org/10.4236/jmmce.2026.143006

Received: February 4, 2026
Accepted: April 5, 2026
Published: April 8, 2026

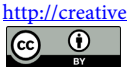

Abstract

This study investigated the stress-strain behavior of additively manufactured IN939 over a temperature range from room temperature to 1000˚C. The results reveal a systematic decrease in ultimate tensile strength (UTS) above 600˚C, accompanied by a non-monotonic variation in yield strength and an abrupt reduction in strain at 800˚C. After completion of the mechanical tests, one side of each fractured specimen was sectioned near the necked region for cross-sectional analysis, while the opposite side was prepared for fractographic examination; both analyses were conducted using scanning electron microscopy (SEM). Failure below 600˚C was characterized by a high γ' precipitate density and predominantly intergranular fracture. The anomalous strain response observed at 800˚C is examined in detail, and a transition in deformation mechanisms associated with temperature-induced changes in the alloy's microstructure is proposed. At 800˚C, fracture surfaces exhibited microcracks, reduced γ' density, micro-scale voids, and small discontinuities. At 1000˚C, incipient melting zones were observed, and no ductile dimples were present.

Keywords

Additive Manufacturing, Ni Superalloys, High Temperature, Stress-Strain, Fractography

1. Introduction

The high-chromium IN939 alloy is extensively used in industrial gas turbines as a structural material for moderate high-temperature applications, particularly in aerospace engines, energy industries, the process industry, oil and gas sectors, and

shipbuilding. Its exceptional oxidation resistance and high creep strength at elevated temperatures make it a vital choice for such applications. IN939 is a precipitation-hardened nickel-based superalloy that has been employed for decades in manufacturing high-temperature cast components, including gas turbine blades, vanes, fuel nozzles, and turbine castings [1] [2]. This alloy performs reliably in combustion turbines operating at temperatures up to 850˚C. However, the development of suitable joining technologies for large structural components in aero engines remains a significant challenge, as highlighted in prior studies [2]. Recent advancements in additive manufacturing (AM) of Ni-based superalloys have shown promise in addressing critical design and engineering challenges. AM technology enables the production of complex geometries, reduces product development cycles, and accelerates time-to-market. Despite these advantages, issues such as micro-cracks and surface oxidation have been observed during production, adversely impacting the mechanical properties of the alloy at high temperatures. These defects are influenced by the precise tolerances of composite elements, particularly zirconium (Zr) and boron (B), which play a crucial role in crack formation [3]. Additionally, anisotropy in the mechanical properties of AM-printed samples has been identified, primarily due to the layer-by-layer deposition process, thermal gradients, and the solidification front. These factors affect the microstructure and, consequently, the failure modes of the material [4]. The primary property of a superalloy used in combustion turbines is its resistance to high-temperature creep. A recent study examined the effects of different heat treatments on IN939 [5]. A lower-temperature treatment (1160˚C for 4 hours, followed by aging at 850˚C for 16 hours) produced small, recrystallized grains between columnar grains. This resulted in large rupture elongation but poor creep life due to the presence of harmful phases such as η. Conversely, a higher-temperature treatment (solution at 1240˚C for 6 hours, followed by aging at 850˚C for 16 hours) significantly improved creep life—2.7 times longer—due to complete recrystallization and increased γ' precipitate size during creep. However, this treatment led to very poor ductility [5]. Further studies revealed that γ' precipitates in cast or wrought IN939 superalloys grow under low-cycle fatigue (LCF) conditions at 790 - 910˚C for up to 1500 hours. The growth rate is primarily controlled by the volume diffusion of alloying elements [6]. Additive manufacturing (AM) techniques produce metallurgical microstructures distinct from those formed through conventional processing, which impacts high-temperature mechanical properties. For example, Inconel 939 processed via selective laser melting (SLM) showed microstructural anisotropy influenced by heat flux during layer-by-layer deposition [7]. Welding studies of IN939 highlighted challenges such as liquation cracking and strain-age cracking in the heat-affected zone (HAZ). These defects were mitigated by post-weld hot isostatic pressing (HIP), which healed cracks but occasionally introduced undesirable new phases [8]. HIP was deemed essential to achieve crack-free joints despite these drawbacks. Non-conventional heat treatments have been explored as alternative methods to restore the microstructure of long-term exposed blades

to normal working conditions. Gonzalez *et al.* [9] found that conventional two-stage heat treatments resulted in a lower volume fraction of primary gamma prime and coarse secondary gamma prime phases, which could negatively impact short-term tensile strength. In contrast, alternative heat treatments successfully restored the microstructure. These studies underscore the potential of thermodynamic processes to enhance the mechanical properties of alloys through tailored microstructural modifications [9]. Marchese *et al.* [10] investigated the microstructure and cracking mechanisms of laser powder bed fusion (LPBF) Inconel 939. They attributed cracking along grain boundaries to high thermal residual stresses caused by rapid cooling and heating rates, as well as the presence of intergranular precipitates. Their findings suggest that reducing powder-related defects could minimize intergranular carbides and cracks. Additionally, their research highlights the effectiveness of hot isostatic pressing (HIP) in consolidating micro-cracks, reducing porosity, and improving the material's mechanical properties [10]. This report investigates the failure mechanisms and deformation modes of additively manufactured (AM) Inconel 939 under stress-strain loading at elevated temperatures. Mechanical properties were evaluated at room temperature and at 600˚C, 700˚C, 800˚C, 900˚C, and 1000˚C. The results show a systematic decrease in ultimate tensile strength (UTS) above 600˚C, along with a non-monotonic variation in yield strength. A pronounced decrease in elongation was observed at 800˚C, followed by a subsequent decline at higher temperatures. The anomalous mechanical response at 800˚C is examined in detail, and a shift in deformation mechanisms associated with temperature-induced changes in the alloy's metallurgical structure is proposed.

2. Experimental

A high-powered EOS M400 Yb-fiber laser, boasting a beam spot quality of 1000 W, a speed of up to seven meters per second, excellent resolution, and precision, was employed in the current study for the fabrication of AMed samples. The IN939 powder, with a spherical shape and a general particle size ranging from 20 to 55 μm, along with its analyzed chemical composition (as detailed in **Table 1**), served as the primary material. **L-PBF** (Laser Powder Bed Fusion) process around 400 W power, 1000 mm/sec. scan speed, 0.1 mm hatch spacing to obtain 20 - 50 μm layer thickness were used to obtain the samples. The AMed samples were built in perpendicular orientation to the beam in two directions- X and Y, and parallel to the beam-Z direction. Cylindrical rod samples derived from the prints underwent a specific heat treatment regime: Solution treatment at 1190˚C for 4 hours, followed by rapid argon cooling to 30˚C - 40˚C. First aging treatment at 1000˚C for 6 hours, followed by rapid argon cooling to 30˚C - 40˚C. and a final aging treatment at 800˚C for 4 hours, followed by rapid argon cooling to room temperature.

Table 1 displays the analyzed chemical composition of the IN939 powder used in the study and some relevant metallurgical data. Following heat treatment, the specimens were machined to form cylindrical ("dog-bone") mechanical property samples, with the following dimensions: 6 mm in diameter, 24 mm gauge length

(4D), and a total length of 75 mm. Tensile tests were conducted using a universal tensile machine and extensimeters, according to ASTM E-8/8M for room temperatures, and ASTM-E21 for the high temperature tests. To minimize oxidation at high temperatures and reduce the effects of dynamic strain aging, a sufficiently high strain rate was employed to ensure reliable stress-strain data. Tests were conducted at 25°C, 600°C, 700°C, 800°C, 900°C, and 1000°C under temperature stability within a few degrees. Deformation was initially performed in strain-controlled mode at a rate of 0.50% per minute up to 1.2% strain (corresponding to the extensometer full scale), after which the control was switched to the frame displacement at rates of 1.60 mm/min and 3.00 mm/min for flat and cylindrical specimens, respectively, until failure. Following the completion of the mechanical tests, one side of each remaining sample was trimmed close to the neck for cross-sectional examination and another side for fractography inspection. The samples were then prepared for SEM metallography inspection along the tensile axis to observe major flow deformation and neck characteristics under high-temperature load. The second remaining sides of the samples were used for fractography investigation at high magnification in a SEM/EDS observe the fracture characteristics in the failure surface. Characterization was conducted using the Thermo-Scientific™ Phenom™ XL G2 scanning electron microscope (SEM).

Table 1. Alloy composition.

Sample/ Elements (wt%)	Ni	Cr	Co	W	Al	Ta	Nb	Ti	Zr	C	B	Traces
Commercial Powder Alloy EOS 9011-0030	Bal.	22.6	19.9	2.06	1.9	1.49	0.98	3.6	0.03	0.15	0.02	Si 0.2 max Others < 100 ppm
Samples Analysis	Bal.	22.8	19.5	1.9	1.9	1.35	0.9	3.6	0.02	0.16	0.004	Ag, Bi, Pb, Se, S, O, N
Conventional Ingot Alloy Standard	Bal.	22 - 22.8	18 - 19.5	1.8 - 2.2	1.8 - 2	1.3 - 1.5	0.9 - 1.1	3.6 - 3.8	0.02 - 0.03	0.13 - 0.17	0.004 - 0.006	Ag, Bi, Pb, Se, S, O, N

3. Results

The mechanical properties—ultimate tensile strength (UTS), yield strength, and strain (ε)—measured at 25˚C, 600˚C, 700˚C, 800˚C, 900˚C, and 1000˚C are summarized in Table 2. The nomenclature used is as follows: σ (UTS) and σ (Yield) correspond to samples printed along the x direction; samples oriented perpendicular to the x direction on the build plate are designated as the y direction, while those aligned with the beam direction are designated as the z direction. "HIP" denotes samples subjected to hot isostatic pressing at 1200 atm and 1000˚C to reduce porosity and microcracks. Results labeled "EOS" refer to data reported in the EOS technical brochure, where build orientations are defined as H (horizontal) and V (vertical) [11]. The values reported in Table 2 represent the average of at least three tests, with a dispersion of less than 3%, and are plotted in Figure 1. Figure 1 shows the evolution of σ (UTS) and σ (Yield) as a function of tempera-

ture, from room temperature up to 1000˚C. Figure 2 presents the corresponding strain over the same temperature range. The curves shown represent best-fit trends for each group of samples with different characteristics and are intended to highlight the overall behavior. No significant differences are observed among the HIP-ed samples, the EOS results, and the other samples. An abrupt decrease in elongation at 800˚C, followed by a pronounced increase at higher temperatures, is observed in Figure 2 and requires further discussion. Post-test SEM metallurgical characterization near the necked region adjacent to the final fracture surface of representative samples tested at different temperatures is presented in Figure 3. Metallographic and fractography images at 700˚C and 900˚C (Figures 3-8) are omitted, as no significant differences were observed compared with those at 600˚C and 800˚C, respectively. All images are presented at the same scale, allowing clear observation of grain boundaries. Cracks are evident at 800˚C and 1000˚C. High-magnification SEM micrographs, enabling observation of precipitates, are shown in Figure 4, highlighting the decrease in γ' precipitate density. SEM fractography of the fracture surfaces, obtained at the same magnification for comparison across different temperatures, are presented in Figures 5-8.

Table 2. Summarized mechanical properties values of Inconel 939 obtained in this work compared to the EOS reported values.

Temp C	25	600	700	800	900	1000
σ_{UTS} x	1545	1402	1115	770	417	209
σ_{UTS} y		1389			418	
σ_{UTS} z	1265	1338	1081	766	401	211
σ_{Yield} x	1085	943	906	553	286	149
σ_{Yield} y		930			289	
σ_{Yield} z	990	893	876	576	287	150
HIP-σ_{UTS}		1380		756		
HIP-σ_{UTS}		922		622		
σ_{UTS} H eos		1420	1050	750	420	
σ_{UTS} V eos		1380	1050	760	380	
σ_{Yield} H eos		1020	870	610	310	
σ_{Yield} V eos		980	910	640	360	
ε-X	10	9.1	5.3	2.5	4.1	11.8
ε-Y		11.3		3.8	4.5	
ε-Z	6.5	15.8	12	5.4	6.5	14
HIP-ε		14.5		4.5		
ε H eos		9	3	1.8	5.5	
ε V eos		13	9.5	5.1	8.75	

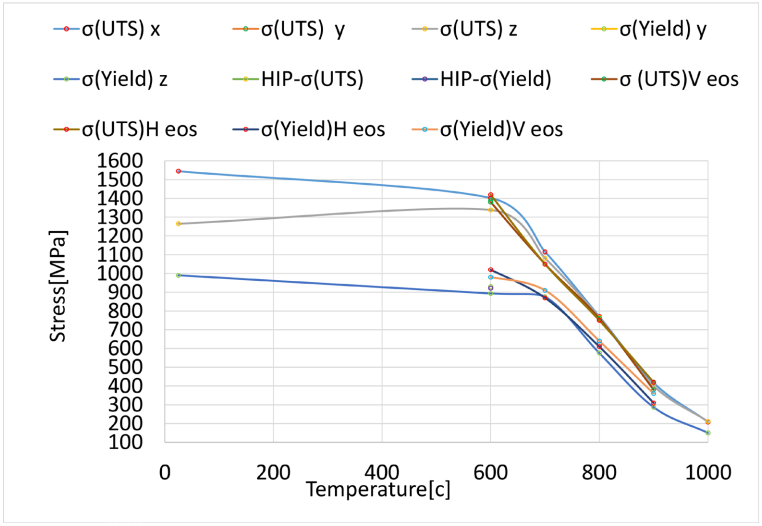

Figure 1. σ_{uts} and the σ_{yield} values from room temperature up to 1000˚C for different sample category. Colored lines represent best fit trend of the results.

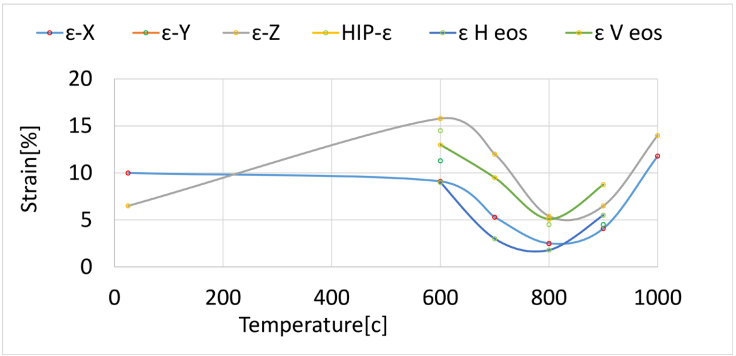

Figure 2. Strain values from room temperature up to 1000˚C for different sample categories. Colored lines represent best fit trend of the results. An abrupt decrease in elongation at 800˚C, followed by a pronounced increase at higher temperatures is observed.

4. Discussion

The deformation mechanisms of Ni-based superalloys, and in some cases Co-based superalloys, are primarily attributed to dislocation shearing of the γ' precipitates via antiphase boundary (APB) cutting under sufficient applied stress, particularly at low temperatures. At higher temperatures, this mechanism is replaced by stacking-fault (SF) formation, which results from the motion of partial dislocations at intermediate temperatures, where dislocations in the matrix bypass precipitates by climb [12]. SF-mediated deformation has been observed in Ni-Co superalloys with increasing temperature and is attributed to the fact that deformation twins are more easily formed than APBs under these conditions. The effects of both precipitate morphology and alloy composition on these mechanisms have been reported in the literature [13]. Simulation results indicate that increasing the tungsten content raises the γ' volume fraction, thereby enhancing creep resistance. Additionally, the addition of tantalum or titanium increases both flow

stress and creep resistance. Alloy IN939 contains 2 wt.% tungsten, 1.4 wt.% tantalum, and 3.6 wt.% titanium, placing it within the same compositional category. Therefore, similar deformation can reasonably be expected, characterized by good creep resistance, *i.e.*, limited deformation at elevated temperatures around 800˚C. In contrast, the high chromium content in IN939 (up to 22.5 wt.%) tends to weaken its creep resistance. This simulation is consistent with the observations presented in **Figure 3** and **Figure 4**. At 800˚C, both figures reveal complementary features: **Figure 3** shows cracks along grain boundaries, highlighting significant grain straightening that can explain the low strain at 800˚C, as shown in **Figure 2**, and the inherent weakness of the grain boundaries. Conversely, **Figure 4** shows a reduction in the number of stable precipitates, evidenced by a lower precipitation density and matrix growth and dislocations bypass precipitates through climb mechanisms. This weakening becomes more pronounced at 1000˚C, where the precipitation density is significantly lower, suggesting that some precipitates may have dissolved at higher temperatures. The weakness of increasing the stain in **Figure 2** at 1000˚C is supported by this explanation. It can be assumed that Ni_3Al and Ni_3Nb precipitates dominate rather than Ni_3Ta and Ni_3Ti, consistent with the simulation's prediction of improved creep resistance [13]. The fractographic analyses shown in **Figures 5-8** further support these observations. The result of small dimples and interconnected discontinuities at room temperature, as presented in **Figure 5**, can be attributed to the small dislocation zone between the precipitates. At higher temperature, as shown in **Figure 6** at 600˚C, cleavages terraces and small dimples around represented. **Figure 3** at this temperature no cracks were found. **Figure 7** presents SEM fractography of the post-load fracture surface at 800˚C, revealing the formation of small holes and surface discontinuities (circled), as well as cracks (arrowed). The relatively low average strain is attributed to the limited presence of dimples on the fracture surface, together with the development of cracks and small holes with sizes of approximately 1 - 2 μm. At 800˚C, an average strain of 3.7% is observed (**Figure 2**). The cracks shown in **Figure 3** and the microcracks observed in **Figure 7**, both at 800˚C, explain the abrupt drop in strain at this temperature. The weakened grain boundaries observed at 800˚C (**Figure 3**), where cracking is pronounced, along with hole formation—assumed to occur around precipitates due to loss of coherency with the matrix—are responsible for the low strain behavior. Recently Fracis *et al.* [14] investigated the high temperature deformation mechanism in polycrystal Ni-base superalloy by neutron diffraction, The elastic lattice strain data gained from the neutron diffraction experiment indicates the γ and γ' deform jointly in the fine γ' microstructure, but not in the medium and coarse γ'. A load transfer between γ and γ' is observed in the elastic lattice strain data for the medium and coarse γ', changing thew deformation behavior, which shows that the same slip system involving single dislocations is active in both phase with continuous stacking faults extending through both phases. In contrast, in coarse γ', stacking faults are restricted to the γ', and the matrix

dislocations do not penetrate the precipitates. Figure 2 presents an increase in the stain at 1000˚C. This behavior can be explained by the observation of the picture in Figure 3 representing the sample post tested at 1000˚C, that shows some cracks created along the grain boundaries but in addition, in Figure 4, in higher magnification at the same temperature, diluted number of precipitates in comparison with the samples at lower temperature. The dissolution of γ' precipitates increase significantly the flow of phase gamma that has lower number of obstacles to be crossed. Moreover, the fractography in Figure 8 presents some incipient melting on the surface. All those factors generously donate to the weakness and the flow of the alloy at 1000˚C. Table 3 summarizes the average strain and the corresponding microscopic observations at temperatures ranging from room temperature to 1000˚C.

Table 3. Average strain and micro-structure observation (SEM).

Temperature [˚C]	25	600	700	800	900	1000
Average Strain [%]	8.2	12.1	5	3.9	5.9	12.9
Microscopy Observation	Intergranular Fracture, High γ' Density	Cleavage terraces, Less γ' Density	Not Observed	Micro-Cracks, Less γ' Density, Holes, discontinuities.	Not Observed	Incipient Melting zones, No dimples.

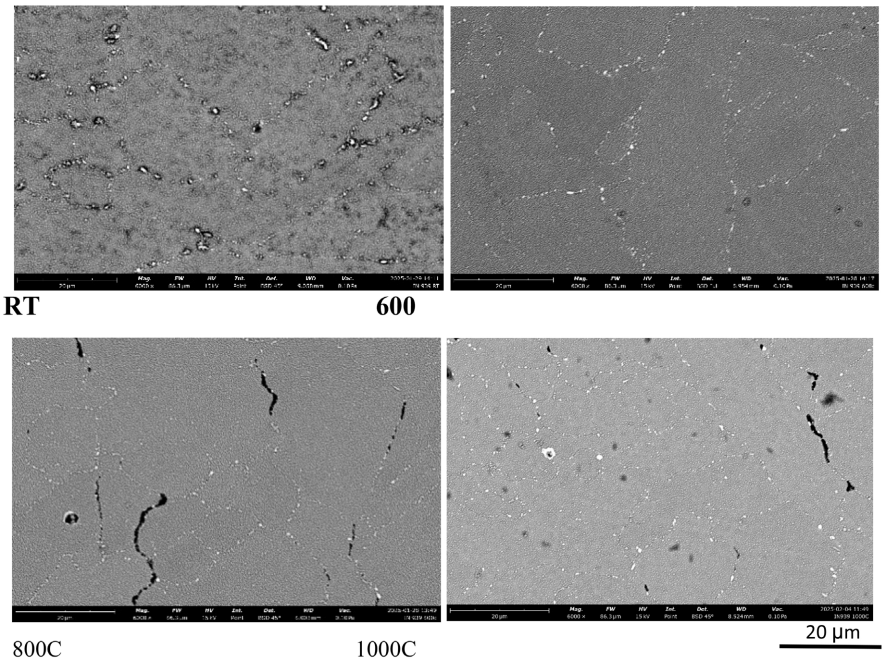

Figure 3. Scanning Electron Microscopy (SEM) images of the post-microstructure near the sample's neck at room temperature (RT), 600˚C, 800˚C, and 1000˚C. Large precipitates are observed along the grain boundaries. While no initial cracks were detected at RT and 600˚C, small open micro-cracks appeared at 800˚C and 1000˚C. (Scall bar-20 microns on the picture).

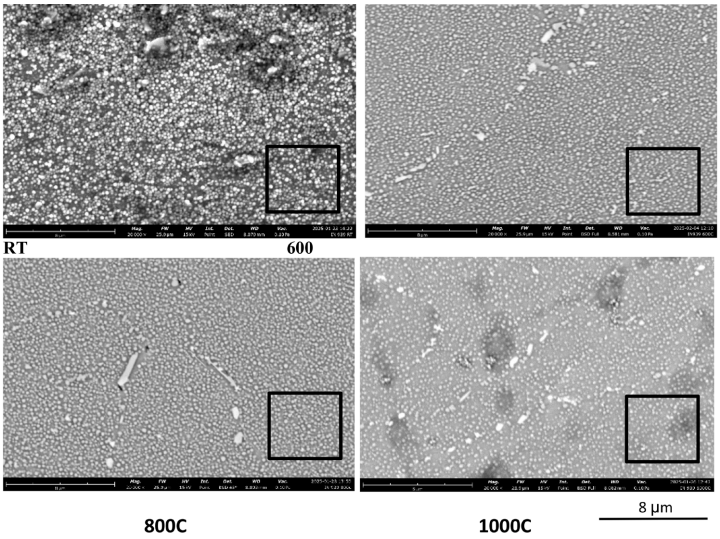

Figure 4. Scanning Electron Microscopy (SEM) images of the samples at room temperature (RT), 600˚C, 800˚C, and 1000˚C. A decrease in intergranular precipitate density is qualitative observed between the pictures, with the highest density at RT, followed by 600˚C and 800˚C (moderate density), and the lowest density at 1000˚C.

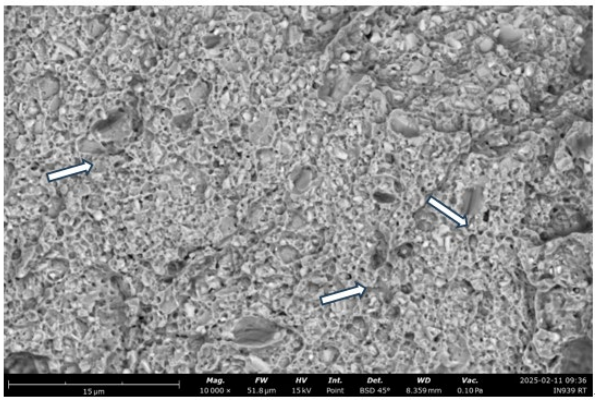

Figure 5. SEM fractography of post load room temperature failure surface—small dimples and interconnected holes (arrows) created during deformation

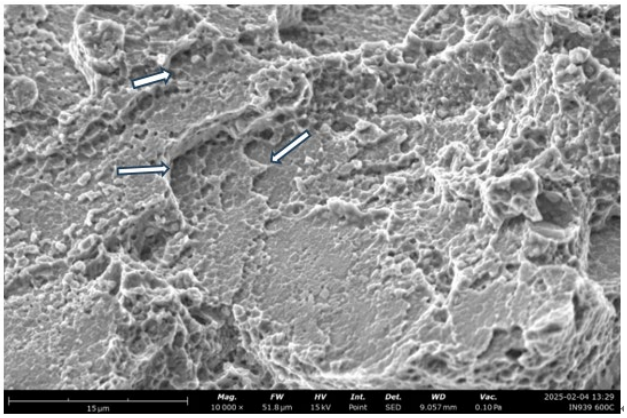

Figure 6. SEM fractography of post load failure surface at 600˚C—cleavage terraces (arrows) small dimples around.

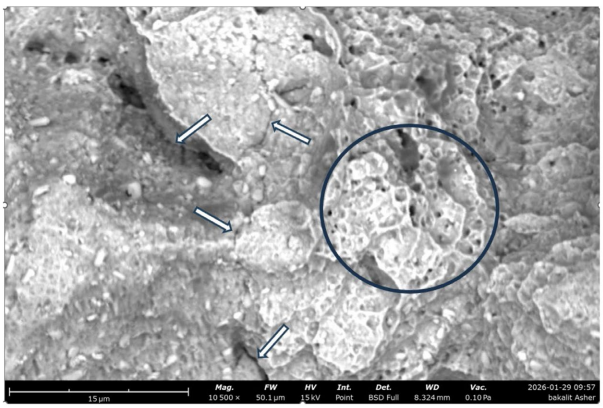

Figure 7. SEM fractography of the post-load failure surface at 800˚C, showing the formation of small holes and surface discontinuities (circled) as well as cracks (arrowed). The observed average strain is attributed to the limited presence of dimples on the fracture surface.

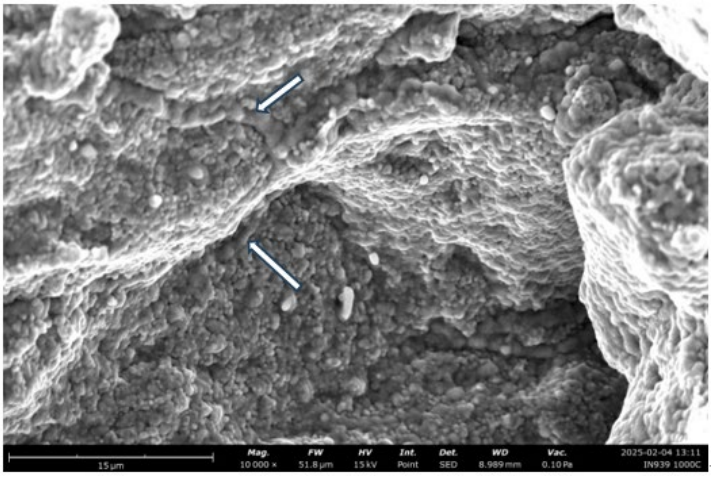

Figure 8. SEM fractography of post load failure surface at 1000˚C—Incipient Melting zones (arrows) but no dimples were observed.

5. Conclusions

The stress-strain behavior of additively manufactured IN939 was investigated over a temperature range from room temperature to 1000˚C. The following conclusions can be drawn:

1) A systematic decrease in ultimate tensile strength (UTS) was observed above 600˚C, accompanied by a non-monotonic variation in yield strength and an abrupt reduction in strain at 800˚C.
2) Cross-sectional microstructural and fractographic analyses near the failure (necking) region were performed using SEM. The deformation behavior below 600˚C was characterized by a high density of γ' precipitates and predominantly intergranular fracture.
3) The low strain observed at 800˚C can be explained by fracture surfaces exhibiting microcracks, a reduced γ' precipitate density, micro-scale voids with

sizes of approximately 1 - 2 μm, and a limited presence of ductile dimples.

4) The high strain observed at 1000˚C can be attributed to the presence of incipient melting zones and the absence of ductile dimple formation.

Further research has to be done for the deeper understanding of the abrupt drop in ductility.

Conflicts of Interest

The authors declare no conflicts of interest regarding the publication of this paper.

References

[1] Wahl, J.B. and Harris, K. (2011) Advanced Ni Base Superalloys for Small Gas Turbines. *Canadian Metallurgical Quarterly*, **50**, 207-214. https://doi.org/10.1179/1879139511y.0000000010

[2] Sjoberg, G., Imamovic, D., Gabel, J., Cabellero, O., Brooks, J.W., *et al.* (2004) Evaluation of the in 939 Alloy for Large Aircraft Engine Structures. *Superalloys* 2004 (*Tenth International Symposium*), Pennsylvania, 19-23 September 2004, 441-450. https://doi.org/10.7449/2004/superalloys_2004_441_450

[3] Shaikh, A.S. (2018) Development of a γ' Precipitation Hardening Ni-Base Superalloy for Additive Manufacturing. Department of Industrial and Materials Science, Chalmers University of Technology, Gothenburg, Sweden.

[4] Moreno, D., Nahmana, Y., Nafman, O., Kam, O., Wolfman, B., Cohen, A.Y., *et al.* (2022) Mechanical Properties, Metallurgical Characteristics and Anisotropy of Additive Manufacturing of 316L. *Journal of Minerals and Materials Characterization and Engineering*, **10**, 209-223. https://doi.org/10.4236/jmmce.2022.102017

[5] Banoth, S., Li, C., Hiratsuka, Y. and Kakehi, K. (2020) The Effect of Recrystallization on Creep Properties of Alloy IN939 Fabricated by Selective Laser Melting Process. *Metals*, **10**, Article 1016. https://doi.org/10.3390/met10081016

[6] Jahangiri, M.R., Arabi, H. and Boutorabi, S.M.A. (2014) Comparison of Microstructural Stability of IN939 Superalloy with Two Different Manufacturing Routes during Long-Time Aging. *Transactions of Nonferrous Metals Society of China*, **24**, 1717-1729. https://doi.org/10.1016/s1003-6326(14)63245-3

[7] Kanagarajah, P., Brenne, F., Niendorf, T. and Maier, H.J. (2013) Inconel 939 Processed by Selective Laser Melting: Effect of Microstructure and Temperature on the Mechanical Properties under Static and Cyclic Loading. *Materials Science and Engineering: A*, **588**, 188-195. https://doi.org/10.1016/j.msea.2013.09.025

[8] Xie, J.L., Ma, Y.C., Xing, W.W., Zhang, L., *et al.* (2018) Heat-Affected Zone Crack Healing in IN939 Repaired Joints Using Hot Isostatic Pressing. *Welding in the World*, **62**, 471-479. https://doi.org/10.1007/s40194-018-0579-5

[9] González, M.A., Martínez, D.I., Pérez, A. and Guajardo, H. (2012) Microstructural Rejuvenation through Non-Conventional Heat Treatments of an Inconel 939 Superalloy. *MRS Proceedings*, **1372**, 89-96. https://doi.org/10.1557/opl.2012.114

[10] Marchese, G., Parizia, S., Saboori, A., Manfredi, D., Lombardi, M., Fino, P., *et al.* (2020) The Influence of the Process Parameters on the Densification and Microstructure Development of Laser Powder Bed Fused Inconel 939. *Metals*, **10**, Article 882. https://doi.org/10.3390/met10070882

[11] EOS-EOS GmbH, Electro Optical Systems (n.d.) Nickel Alloy IN939 Excellent High Temperature Performance with Corrosion Resistance.

[12] Hu, R., Zhao, J.Z., Yang, C., Du, J.H., Luo, X., Bi, Z., *et al.* (2022) Temperature Effects on the Deformation Mechanisms in a Ni-Co-Based Superalloys. *Crystals*, **12**, Article 1409. https://doi.org/10.3390/cryst12101409

[13] Keshavarz, S., Campbell, C.E. and Reid, A.C.E. (2024) Advanced Computational Analysis of Cobalt-Based Superalloys through Crystal Plasticity. *Materials*, **17**, Article 2458. https://doi.org/10.3390/ma17102458

[14] Francis, E.M., Grant, B.M.B., Fonseca, J.Q.D., Phillips, P.J., Mills, M.J., Daymond, M.R., *et al.* (2014) High-Temperature Deformation Mechanisms in a Polycrystalline Nickel-Base Superalloy Studied by Neutron Diffraction and Electron Microscopy. *Acta Materialia*, **74**, 18-29. https://doi.org/10.1016/j.actamat.2014.04.028